excitance of about 0.004 W/m^2. Since the error in instrument noise decreases as the square root of the number of samples (*12*), we are able to reduce this source of noise significantly below that of the signal we wish to detect. For example, about 100 northbound observations were made each day by Nimbus 3 (*11*). Thus, the daily error in excitance due to instrument noise was about 0.0004 W/m^2, a value that places very little limitation on detection. A second source of instrument noise arises from using a series of different detectors over a long period. Each new satellite will carry a new instrument with different noise characteristics and, more importantly, a different absolute radiometric calibration. Solutions to this problem could involve looking at the ratio of the change between spectral channels, which might eliminate errors due to the calibration of the particular instrument, or using one instrument aboard the space shuttle over a long period. Thus we feel that errors due to the instrument will not severely limit the detection of changes in excitance.

Variations in the outgoing longwave flux due to the natural variability of the atmospheric thermal structure are also a source of noise. The standard deviations of radiance for the Nimbus 3 and Nimbus 6 satellites have been reported by Fritz and Soules (*11*) and Barnett (*13*), respectively. These studies indicate a standard deviation in radiance of 1 mW/m^2-sr-cm^{-1}, which corresponds to a standard deviation in excitance of 0.016 W/m^2, for low and mid-latitudes in all months except December, January, and February. Higher latitudes (above 60°) exhibit much greater variability in radiance and would make detection of the signal due to increased CO_2 very difficult. Thus temporal averages should be confined to daily averaged measurements for nonwinter months. Spatial averaging should not include latitudes above 60° in either hemisphere.

Figures 1 and 2 imply changes in excitance at 667 cm^{-1} of -0.06 W/m^2. Thus the signal of change in excitance due to doubled CO_2 is about four times larger than the noise due to natural variability. This analysis has considered changes due to a doubling of atmospheric CO_2; obviously the natural variation will place limitations on the specific time in which a climatic signal is detectable, as is the case for any other detection method (*2*, *14*).

This method for the 500 to 800 cm^{-1} spectral region can be used to detect changes in outgoing longwave flux, which in turn signify a change in the thermal structure of the stratosphere, in CO_2, or in both. Furthermore, perturbations of the stratospheric temperature structure are not only confined to increases in CO_2. Increases in other trace gases can also affect the radiative balance of the atmosphere (*2*, *15*). In particular, studies of reduced stratospheric ozone due to increases in chlorofluoromethanes (*15*) suggest that temperature decreases on the order of those due to doubled CO_2 may result. It is essential that other spectral regions be monitored in order to identify the causes of the observed changes in the atmosphere's thermal structure.

J. T. KIEHL

National Center for Atmospheric Research, Boulder, Colorado 80307

References and Notes

1. V. Gornitz, S. Lebedeff, J. Hansen, *Science* **215**, 1611 (1982); J. Hansen, D. Johnson, A. Lacis, S. Lebedeff, P. Lee, D. Rind, G. Russell, *ibid*. **213**, 957 (1981); G. Kukla and J. Gavin, *ibid*. **214**, 497 (1981).
2. R. A. Madden and V. Ramanathan, *ibid*. **209**, 763 (1980).
3. J. T. Houghton, *The Physics of the Atmosphere* (Cambridge Univ. Press, Cambridge, Mass., 1977), p. 149.
4. R. A. McClatchey, R. W. Fenn, J. E. A. Selby, F. E. Volz, J. S. Garing, *U.S. Air Force Cambridge Res. Lab. Environ. Res. Pap. No. 254* (1971).
5. W. Malkmus, *J. Opt. Soc. Am.* **57**, 325 (1967).
6. R. E. Roberts, J. E. A. Selby, L. M. Biberman, *Appl. Opt.* **15**, 1085 (1976).
7. Calculations with two times the amount of water vapor for the doubled CO_2 cases change the results shown in Fig. 2 only slightly. The excitance due to tropospheric water vapor in the far spectral regions does not change since the lines in this region are saturated.
8. T. H. Vonder Haar and V. E. Suomi, *J. Atmos. Sci.* **28**, 305 (1971).
9. V. Ramanathan and R. E. Dickinson, *ibid*. **36**, 1084 (1979).
10. S. Manabe and R. T. Wetherald, *ibid*. **37**, 99 (1980); W. M. Washington and G. A. Meehl, *J. Geophys. Res.* **88**, 6600 (1983).
11. S. Fritz and S. D. Soules, *Mon. Weather Rev.* **100**, 582 (1972).
12. W. Mendenhall and R. L. Scheaffer, *Mathematical Statistics with Applications* (Duxbury, Belmont, Calif., 1973), pp. 185–191.
13. J. J. Barnett, *Philos. Trans. R. Soc. London Ser. A* **296**, 41 (1980).
14. E. S. Epstein, *J. Appl. Meteorol.* **21**, 1172 (1982).
15. V. Ramanathan, in *Interactions of Energy and Climate*, W. Bach, J. Pankrath, J. Williams, Eds. (Reidel, Boston, 1980), p. 269.
16. I thank V. Ramanathan for discussions which initiated this work. I also wish to thank W. W. Kellogg, W. Washington, and P. Chylek for helpful comments on an earlier draft of this manuscript. I am especially grateful for many stimulating discussions and helpful suggestions from J. A. Coakley, Jr. The National Center for Atmospheric Research is sponsored by the National Science Foundation.

16 May 1983

Determining the Solar Wind Speed Above Active Regions Using Remote Radio-Wave Observations

Abstract. *A new technique has made it possible to measure the velocity of portions of the solar wind during its flow outward from the sun. This analysis utilizes spacecraft (ISEE-3) observations of radio emission generated in regions of the solar wind associated with solar active regions. By tracking the source of these radio waves over periods of days, it is possible to measure the motion of the emission regions. Evidence of solar wind acceleration during this outward flow, consistent with theoretical models, has also been obtained.*

The spiral shape of the interplanetary magnetic field lines is a consequence of the outward flow of the solar wind and the solar rotation. Above about 10 solar radii ($R_{\odot}$), the magnetic field is carried out with the expanding plasma and its lines of force take a spiral shape first predicted by Parker (*1*; *2*, pp. 41–72). This shape has been confirmed by in situ space probe measurements and also by radio tracking of solar energetic particles responsible for the type III burst radiation (*3*).

Solar type III radio bursts are produced by packets of energetic electrons that are accelerated in the low corona or chromosphere and travel outward through the corona and interplanetary space. At each altitude, the electrons excite plasma waves that are converted into electromagnetic waves at the plasma frequency or at its second harmonic (*4*).

During its first 4 years of operation, the ISEE-3 spacecraft (*5*) has been stationed close to the libration point situated ~ 240 earth radii toward the sun. This location is particularly good for radio observations since it is both far from the sources of the earth's radio noise and it allows almost continuous observations. The Paris Observatory–National Aeronautics and Space Administration Goddard Space Flight Center radio experiment on board the ISEE-3 spacecraft (*6*) uses the spin modulation of the received data resulting from the rotation of the spacecraft dipole antenna to deduce the direction of a compact radio source. The technique (*3*, *7*) has been used to map the trajectories of intense isolated type III bursts through the interplanetary medium (*3*).

Hectometer-wavelength type III solar storms have been discovered during the last solar cycle as a result of RAE-1 (Radio Astronomy Explorer) satellite observations (*8*, *9*). They consist of hundreds of individual type III storm bursts emitted per hour during several consecutive days. They may even recur during two or more solar rotations of the associated active region. They are not directly associated with solar flares, in contrast to most isolated large type III bursts. A preliminary analysis of the ISEE-3 radio data (*10*) shows that type III solar storms are a common extension of the solar activity into interplanetary space: the hectometer-kilometer interplanetary type III storms (IP storms) are the signature of long-lasting streams of electrons accelerated or released above the active regions in a narrow altitude range (1.5 to 2.5 $R_{\odot}$). These electron streams in the solar wind are traced by their radio emission as far out as 0.8 astronomical unit from the sun (1 A.U. = 215 $R_{\odot}$).

We have developed a new technique to determine the solar wind speed within the plasma elements responsible for the radio emission. The data utilized are the ISEE-3 measurements of solar elongation of radio sources averaged over successive 30-minute intervals (Fig. 1). The measured elongations are corrected for the galactic background according to a method discussed by Fainberg (*7*). For each observing frequency, we can see the east-to-west motion of the IP storm region as it crosses the line of sight of ISEE-3 to the sun. The different slopes on Fig. 1 (especially between 30 June and 3 July 1979) are due to a foreshortening effect. The sources that are closer to the observer (at lower frequencies) cross the line of sight with a higher angular velocity than the distant ones (at higher frequencies). This geometrical effect allows us to locate the distance from the spacecraft to the emission region directly. In other words, we are able to determine the emission levels just from the analysis of the slopes of the source solar elongation profiles. In addition, we observe that the central meridian crossing occurs later at lower frequencies. This delay is a direct measure of the time it takes the solar wind to flow between the levels determined from the slope analysis. This is demonstrated in Fig. 2, which also sketches the spiral shape of the average interplanetary magnetic line of force in the IP storm region at three different times in the course of the storm.

The result of this analysis is shown in Fig. 3 for the IP storm observed from 29 June to 4 July 1979. Each point in Fig. 3 results from measurements at one radio frequency sampled by our instrument. Since we are using all data within 1 or 2 days around central meridian passage and since the earth moves only by a few degrees over the period when the measurements are made, we are viewing essentially the same solar wind portion as it moves outward from about 40 to 150 $R_{\odot}$.

The data in Fig. 3 suggest an acceleration of the solar wind since the curvature is positive. In order to further check this point, we have analyzed 20 IP storms, using the above technique, and we have used a least squares fit of the distance-time data to a quadratic curve. The results show that most storms exhibit a solar wind acceleration with a broad distribution centered at 0.3 m sec^{-2}, in good agreement with theoretical results in this distance range (*11*).

Theoretical models predict that the acceleration decreases with distance from the sun (*2*, p. 75; *11*). A simple empirical relation $V(R) = aR^{1/4}$ (*12*) fits Parker's theoretical curves for $V(R)$ for various coronal conditions (a is an empirical parameter related to the solar wind speed V, and R is the distance from the sun). The line in Fig. 3 is the least squares fit of our data to this model. It corresponds to an increase in velocity from about 250 km sec^{-1} at 50 $R_{\odot}$ to 330 km sec^{-1} at 150 $R_{\odot}$. The extrapolated speed is 360 km sec^{-1} at the earth. In situ observations show that, within a few days of the arrival of this storm, the velocity ranges from 350 to 450 km sec^{-1} (*13*).

From a preliminary comparison between solar wind speeds derived from these observations and in situ measurements at 1 A.U., we sometimes find substantial differences in speed. Such

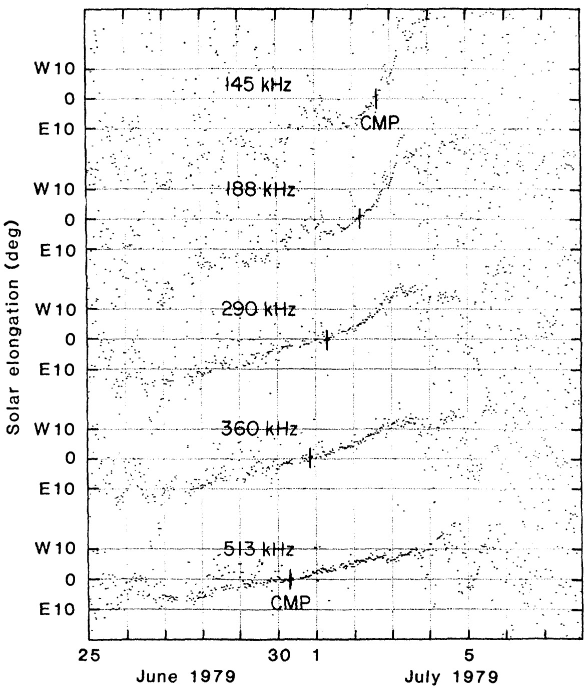

Fig. 1. Time variation of the solar elongation of a typical interplanetary type III storm at several frequencies. Each dot represents the average taken over a 30-minute interval. The drift is produced by the solar rotation, and it is faster for lower frequencies when the radio source is closer to the observer. The time of central meridian passage (*CMP*) occurs later at lower frequencies as a result of the spiral shape of the magnetic field lines.

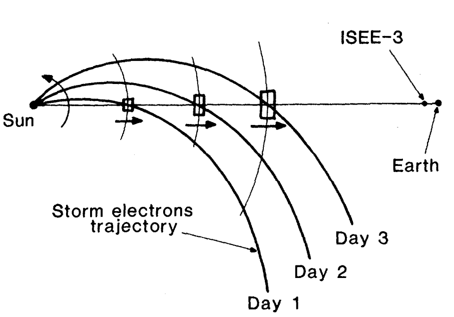

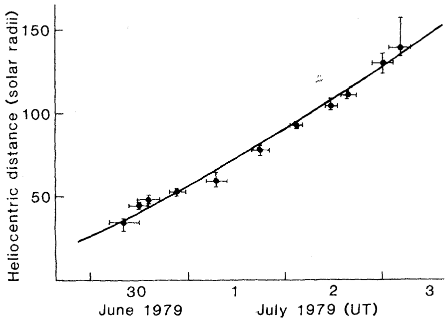

Fig. 2 (left). Geometry of the observing conditions showing that, when the measurements are taken near central meridian passage, the radio sources track the same region of solar wind as it moves outward. Fig. 3 (right). Heliocentric distance of the radio sources at different frequencies, deduced from the rate of change of the solar elongation, as a function of the date of central meridian passage for the storm shown in Fig. 1. A straight line corresponds to a constant speed, and a positive curvature corresponds to an acceleration. The solid line corresponds to the least squares fit to the expression $R(t) = c(t - t_0)^{4/3}$ (where t is the time, t_0 is a reference time, and c is a constant related to a), which approximates Parker's theoretical model of the solar wind expansion (*1*, *2*).

differences may be due to the following facts, which make a detailed comparison difficult. First, it is necessary to extrapolate our observation to 1 A.U. Second, our results correspond to averages taken over the dimension of the radio source region. Third, our observations apply to regions which may have a considerable extent out of the ecliptic plane and for which the solar wind may be substantially different. Fourth, we must assume that the conditions defining the storm region remain constant during 2 to 3 days when we measure the rate of the solar elongation of the radio sources. Such an assumption has already been verified during an earlier IP storm (*9*).

This new technique, which enables us to track for the first time the solar wind expansion by use of the ISEE-3 radio observations of IP storms, works because of the long duration of the IP storms (several days). By comparison with the earlier analysis of radio measurements from the IMP-6 (Interplanetary Monitoring Platform) satellite (*3*), our technique requires few ad hoc assumptions. We derive the movement of the solar wind plasma in the earth's direction without an assumption of an average interplanetary density model. Our first results show a slight acceleration from 50 to 150 $R_{\odot}$, consistent with the results predicted by theoretical models of the solar wind.

J.-L. BOUGERET*
J. FAINBERG
R. G. STONE
Laboratory for Extraterrestrial Physics, NASA/Goddard Space Flight Center, Greenbelt, Maryland 20771

References and Notes

1. E. N. Parker, *Astrophys. J.* **128**, 664 (1958).
2. ———, *Interplanetary Dynamical Processes* (Interscience, New York, 1963).
3. J. Fainberg, L. G. Evans, R. G. Stone, *Science* **178**, 743 (1972).
4. M. L. Goldstein, R. A. Smith, K. Papadopoulos, *Astrophys. J.* **234**, 683 (1979).
5. The International Sun-Earth Explorer spacecraft is a joint project of NASA and the European Space Agency.
6. R. Knoll *et al.*, *IEEE Trans. Geosci. Electron.* **GE-16**, 199 (1978).
7. J. Fainberg, *NASA Tech. Mem. 80598* (1979).
8. ——— and R. G. Stone, *Sol. Phys.* **15**, 222 (1970).
9. ———, *ibid.*, p. 433.
10. J.-L. Bougeret, J. Fainberg, R. G. Stone, *Astron. Astrophys.*, in press.
11. M. Dryer, *Space Sci. Rev.* **33**, 233 (1982), table I, p. 237.
12. L. F. Burlaga, *J. Geophys. Res.* **72**, 4449 (1967).
13. J. H. King, *Interplanetary Medium Data Book—Supplement 2* (Publication NSSDC 83-OX, National Space Science Data Center, NASA, Greenbelt, Md., 1983).
14. We acknowledge useful discussions with L. F. Burlaga and K. W. Ogilvie.

* Research associate with the Astronomy Program, University of Maryland, on leave from Laboratoire Associe au Centre National de la Recherche Scientifique No. 264, Observatoire de Paris, France.

26 April 1983; accepted 6 July 1983

A Micromechanical Contribution to Cochlear Tuning and Tonotopic Organization

Abstract. *The response properties of hair cells and nerve fibers in the alligator lizard cochlea are frequency selective and tonotopically organized with longitudinal position in the organ. The lengths of the hair-cell hair bundles also vary monotonically with longitudinal position. In this study, quantitative measurements were made of the motion of individual hair bundles in an excised preparation of the cochlea stimulated at auditory frequencies. The angular displacement of hair bundles is frequency selective and tonotopically organized, demonstrating the existence of a micromechanical tuning mechanism.*

One of the persistent problems in auditory physiology has been to identify mechanisms responsible for sharp frequency selectivity (tuning) and tonotopic organization in the responses of cochlear hair cells and nerve fibers (*1*). Controversy exists concerning the nature of mechanisms that might supplement the tuning of basilar-membrane motion to provide sharper tuning of hair-cell and nerve-fiber responses (*2*). In light of recent measurements of basilar-membrane motion (*3*), it is unclear to what extent such additional tuning mechanisms are required in the mammalian cochlea; however, in the cochlea of one reptile, the alligator lizard (*Gerrnonotus multicarinatus*), there is a clear difference between basilar-membrane tuning and the tuning of both hair-cell receptor potential and nerve-fiber average discharge rate (*4–7*). Hair-cell and nerve-fiber responses are relatively sharply tuned and tonotopically organized with longitudinal position in the organ (*6, 7*), but the motion of the basilar membrane seems to be neither sharply tuned nor tonotopically organized (*8*). Therefore, this organ must contain an additional mechanism, between basilar-membrane motion and the generation of the hair-cell receptor potential, which produces both additional tuning and tonotopic organization. This mechanism has been proposed to reside in mechanically resonant properties of the hair-cell hair bundles (*4, 5, 9*). We now show that such a micromechanical mechanism exists, that tuning and tonotopic organization occur at the mechanical input to the hair cells.

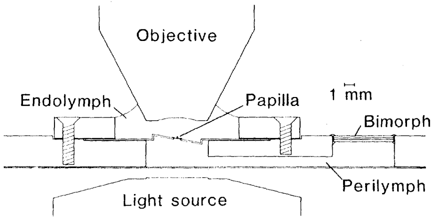

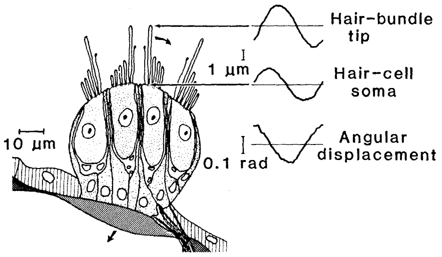

Fig. 1 (left). The experimental chamber. The dissected organ is cemented with Histoacryl adhesive across a hole in a partition separating two fluids. An artificial endolymph (2 m*M* Na^+, 169 m*M* K^+, 2 m*M* Ca^{2+}, 3 m*M* D-glucose, 5 m*M* Hepes buffer; *p*H 7.3) bathes the top (hair-bundle) surface of the organ; an artificial perilymph (168 m*M* Na^+, 2 m*M* K^+, 2 m*M* Ca^{2+}, 3 m*M* D-glucose, 5 m*M* Hepes buffer; *p*H 7.3) bathes the bottom (basilar membrane) surface. The organ is stimulated by driving the fluid in the bottom compartment at frequencies between 1 and 4 kHz with a piezoelectric bimorph element. The resulting motion of the organ is observed from above with differential interference contrast optics and recorded on videotape. Xenon-flash stroboscopic illumination is used to slow or stop the apparent motion of the organ. Fig. 2 (right). Method of quantitative measurement of hair-bundle motion. The schematic cross section of the organ [adapted from Mulroy (*10*)] shows four hair cells and the associated supporting cells resting on the basilar membrane (gray hatching). In response to stimulation, the basilar membrane appears to pivot (lower arrow), while the receptor organ rocks from side to side in the plane of the cross section. Motion of the receptor organ in this plane deflects hair bundles along their axes of morphological symmetry (upper arrow); such displacements produce maximal receptor potentials in hair cells (*17*). Stimulus-induced motions of the hair-bundle tips and hair-cell somata along the axis of symmetry were measured by processing video pictures of the moving organ with an electronic edge detector that tracked a contrast edge in the image (for example, the edge of a moving hair bundle) through a series of frames and produced an output proportional to the position of the edge. By focusing on the organ at different depths, the motion of the tip of a hair bundle (top waveform) and of the soma (middle waveform) were measured for an individual hair cell. The angular displacement of the hair bundle with respect to the soma (bottom waveform) was computed by subtracting waveforms of hair-bundle tip and somatic displacement and dividing the result by the height of the hair bundle, measured with the calibrated focusing knob of the microscope.